






Visualizing quantum phases and identifying quantum phase transitions by nonlinear dimensional reduction

Yuan Yang ^{1,*} Zheng-Zhi Sun ^{1,*} Shi-Ju Ran ^{2,†} and Gang Su ^{3,1,‡}

¹*School of Physical Sciences, University of Chinese Academy of Sciences, P.O. Box 4588, Beijing 100049, China*

²*Department of Physics, Capital Normal University, Beijing 100048, China*

³*Kavli Institute for Theoretical Sciences, and CAS Center for Excellence in Topological Quantum Computation, University of Chinese Academy of Sciences, Beijing 100190, China*

 (Received 22 June 2020; revised 10 December 2020; accepted 23 January 2021; published 2 February 2021)

Identifying quantum phases and phase transitions is key to understanding complex phenomena in statistical physics. In this work, we propose an unconventional strategy to access quantum phases and phase transitions by visualization based on the distribution of ground states in Hilbert space. By mapping the quantum states in Hilbert space onto a two-dimensional feature space using an unsupervised machine learning method, distinct phases can be directly specified and quantum phase transitions can be well identified. Our proposal is benchmarked on gapped, critical, and topological phases in several strongly correlated spin systems. As this proposal directly learns quantum phases and phase transitions from the distributions of the quantum states, it does not require priori knowledge of order parameters of physical systems, which thus indicates a perceptual route to identify quantum phases and phase transitions particularly in complex systems by visualization through learning.

DOI: [10.1103/PhysRevB.103.075106](https://doi.org/10.1103/PhysRevB.103.075106)

I. INTRODUCTION

Studying quantum phases and phase transitions in many-body systems belongs to the most challenging topics in contemporary physics. The characterization of quantum phases within Landau paradigm [1,2] often requires certain prior knowledge of order parameters. For the phases beyond the Landau paradigm [3], one of the main challenges is how to find proper “order parameters,” which might be nonlocal or could not be represented by any observables, to characterize the quantum phases [4]. While conventional approaches usually rely on the priori knowledge and human wisdom, machine learning (ML) provides an alternative way by training an ML model based on certain given relevant data. One popular strategy is to utilize a machine learning model (such as neural network or Boltzmann machine) as the classifier to identify the phases of many-body systems [5–8]. In these cases, a supervised learning process is usually involved.

Another promising direction is to incorporate with the unsupervised learning schemes to reveal the phases. For instance, Wang *et al.* uses a linear dimensionality reduction algorithm known as principle component analyses (PCA) [9] to identify the thermodynamic phase transitions of classical Ising models [10]. One advantage of the unsupervised learning schemes is that less prior knowledge is required, such as the knowledge on the number of phases and the data for training the model [10–21]. However, the unsupervised learning of quantum phases are particularly challenging, mainly due to the exponentially large Hilbert space. In the previous works, one usually implements Monte Carlo samplings to

solve this issue [10–15]. It is strongly desired to develop novel, efficient, and simple schemes to learn quantum phases via an unsupervised process.

In this work, we propose an unconventional approach to access the physical information of quantum phases and phase transitions of many-body systems. Our proposal is to probe the ground-states (GS) distribution in Hilbert space (denoted as \mathcal{H}) by the unsupervised nonlinear dimensionality reduction (DR) scheme [19–24] known as t -distributed stochastic neighbor embedding (t -SNE) [14,25–27]. Such a DR algorithm maps the quantum states from \mathcal{H} to a two-dimensional (2D) feature space (denoted as \mathcal{R}^2) by stochastically maximizing the similarity between the GS distribution in \mathcal{H} and that in \mathcal{R}^2 . By simply viewing the distribution in \mathcal{R}^2 using naked eyes or employing classical algorithms such as k -means [28], we show that the ground states can be readily classified into correct phases and the critical points of quantum phase transitions can be reliably determined. Our proposal is benchmarked on one-dimensional (1D) quantum lattice models, where we visualize that the quantum states in various phases (including gapped, critical, and topological phases) cluster into different patterns in \mathcal{R}^2 , and the phase transitions can be directly specified. Different from the conventional approaches in many-body physics where one usually focuses on order parameters, entanglements and so on, our work poses a new way to view quantum phases from mutual distances between them. In addition, the present proposal works well not only for quantum data like quantum states but also for classical data like image classification.

II. QUANTUM PHASE VISUALIZATION

The central idea of our scheme is to visualize the quantum states by reducing the dimensionality of the exponentially large Hilbert space spanned by the quantum states to two

*These two authors contributed equally to this work.

†sjran@cnu.edu.cn

‡gsu@ucas.ac.cn

dimensionality using t -SNE. The t -SNE is a nonlinear DR method that has been widely used in machine learning to visualize high-dimensional data [26]. Consider a quantum Hamiltonian $\hat{H}(\alpha)$ with α a physical parameter (e.g., a coupling constant or magnetic field), where we suppose a phase transition occurs at $\alpha = \alpha_c$. When α changes continuously, the GS's (denoted as $\{|\psi^\alpha\rangle\}$) form a manifold in the Hilbert space \mathcal{H} . To proceed, we sample N states by taking N different values of α . These quantum states are distributed within the manifold.

Given the data in a high-dimensional space (e.g., the GS's $\{|\psi^\alpha\rangle\}$ in the Hilbert space \mathcal{H}), one can define the joint probability for each pair of the data ($|\psi^\alpha\rangle$ and $|\psi^{\alpha'}\rangle$) as

$$P(D_{\alpha,\alpha'}^{\mathcal{H}}) = \frac{P(\alpha|\alpha') + P(\alpha'|\alpha)}{2N}, \quad (1)$$

where N is the number of states and the conditional probability is defined by the distances as

$$P(\alpha|\alpha') = \frac{\exp[-(D_{\alpha,\alpha'}^{\mathcal{H}})^2/2\sigma_\alpha^2]}{\sum_{\beta \neq \alpha} \exp[-(D_{\alpha,\beta}^{\mathcal{H}})^2/2\sigma_\alpha^2]}, \quad (2)$$

with $\{\sigma_\alpha\}$ the hyper-parameters in t -SNE, and $D_{\alpha,\alpha'}^{\mathcal{H}}$ is the measure of the distances in \mathcal{H} , which can be chosen as different quantities (see below).

One usually does not directly control $\{\sigma_\alpha\}$ but define a quantity named as *perplexity* \mathcal{P} . Given \mathcal{P} , one can perform the binary search to determine $\{\sigma_\alpha\}$ that satisfy

$$\log_2 \mathcal{P} = - \sum_{\alpha'} P(\alpha'|\alpha) \log_2 P(\alpha|\alpha'), \quad (3)$$

The perplexity controls how nonlocally that one state is related to others in the joint probability distributions. More results are provided in Sec. V to show the robustness of phase visualization with different perplexities.

To map $\{|\psi^\alpha\rangle\}$ onto $\{\mathbf{y}^\alpha\}$ in \mathcal{R}^2 , one can randomly initialize $\{\mathbf{y}^\alpha\}$ and define the joint probabilities $\{P(D_{\alpha,\alpha'}^{\mathcal{R}})\}$ as the Student t -distribution [26]

$$P(D_{\alpha,\alpha'}^{\mathcal{R}}) = \frac{[1 + (D_{\alpha,\alpha'}^{\mathcal{R}})^2]^{-1}}{\sum_{\beta \neq \alpha} [1 + (D_{\alpha,\beta}^{\mathcal{R}})^2]^{-1}}, \quad (4)$$

where the measure of the distances in \mathcal{R}^2 is chosen to be the Euclidean distances $D_{\alpha,\alpha'}^{\mathcal{R}} = \|\mathbf{y}^\alpha - \mathbf{y}^{\alpha'}\|$.

To capture $\{|\psi^\alpha\rangle\}$ by $\{\mathbf{y}^\alpha\}$, the strategy of t -SNE is to optimize $\{\mathbf{y}^\alpha\}$ by minimizing the Kullback-Leibler (KL) divergence [29] between $\{P(D_{\alpha,\alpha'}^{\mathcal{H}})\}$ and $\{P(D_{\alpha,\alpha'}^{\mathcal{R}})\}$. The KL divergence is defined as

$$\text{KL}(\mathcal{H}, \mathcal{R}^2) = \sum_{\alpha,\alpha'} P(D_{\alpha,\alpha'}^{\mathcal{H}}) \log \frac{P(D_{\alpha,\alpha'}^{\mathcal{H}})}{P(D_{\alpha,\alpha'}^{\mathcal{R}})}. \quad (5)$$

The gradients by varying \mathbf{y}^α are given by

$$\frac{\delta \text{KL}(\mathcal{H}, \mathcal{R}^2)}{\delta \mathbf{y}^\alpha} = 4 \sum_{\alpha'} \frac{[P(D_{\alpha,\alpha'}^{\mathcal{H}}) - P(D_{\alpha,\alpha'}^{\mathcal{R}})](\mathbf{y}^\alpha - \mathbf{y}^{\alpha'})}{1 + (D_{\alpha,\alpha'}^{\mathcal{R}})^2}. \quad (6)$$

One may use a gradient-descent approach to minimize $\text{KL}(\mathcal{H}, \mathcal{R}^2)$. The converged \mathbf{y}^α are considered as the embedding of ψ^α in \mathcal{R}^2 where the mutual distances among $\{|\psi^\alpha\rangle\}$ in \mathcal{H} are optimally retained by \mathbf{y}^α .

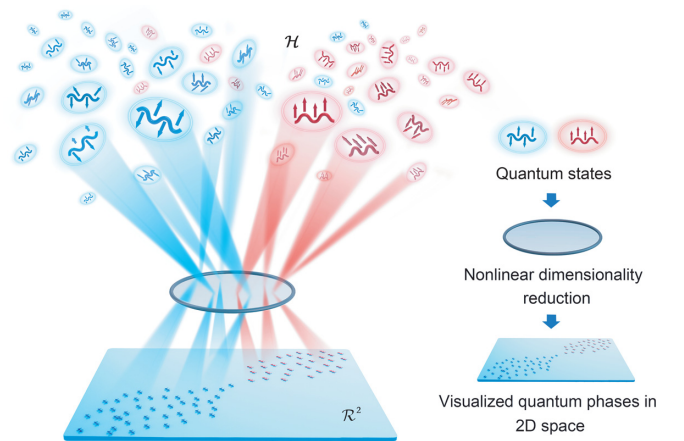


FIG. 1. Visualizing quantum states via an unsupervised nonlinear dimensionality reduction: An illustration. The ground states in the Hilbert space \mathcal{H} of exponentially large dimensionality can be mapped onto a two-dimensional feature space \mathcal{R}^2 via t -SNE, taking negative logarithmic fidelity to measure the distance between two quantum states. Different points in the feature space represent the ground states at different physical parameters in the Hamiltonian. The quantum phases and phase transitions can be clearly specified through the visualized distribution of the states in \mathcal{R}^2 .

To visualize the distribution of certain given GS's $\{|\psi^\alpha\rangle\}$, we invoke the recipe of t -SNE and map the states onto the vectors $\{\mathbf{y}^\alpha\}$ living in a 2D feature space \mathcal{R}^2 , i.e., $|\psi^\alpha\rangle \xrightarrow{f} \mathbf{y}^\alpha$ with $\mathbf{y}^\alpha = [y_1^\alpha, y_2^\alpha]$ a two-component vector and f a nonlinear map from \mathcal{H} to \mathcal{R}^2 (Fig. 1). It should be noted that $\{\mathbf{y}^\alpha\}$ in \mathcal{R}^2 is randomly initialized. To be specific, we start from N given states $\{|\psi^\alpha\rangle\}$ and define the joint probability distributions $\{P(D_{\alpha,\alpha'}^{\mathcal{H}})\}$ based on the distances $D_{\alpha,\alpha'}^{\mathcal{H}}$ between any two of states $|\psi^\alpha\rangle$ and $|\psi^{\alpha'}\rangle$. Then, we randomly initialize N vectors $\{\mathbf{y}^\alpha\}$ in \mathcal{R}^2 and define joint probability distributions $\{P(D_{\alpha,\alpha'}^{\mathcal{R}})\}$ based on the distances $D_{\alpha,\alpha'}^{\mathcal{R}}$ between any two vectors in $\{\mathbf{y}^\alpha\}$. We choose the Euclidean distance as $D_{\alpha,\alpha'}^{\mathcal{R}}$, and the negative logarithmic fidelity (NLF) [30,31]

$$D_{\alpha,\alpha'}^{\mathcal{H}} = -\log(|\langle \psi^\alpha | \psi^{\alpha'} \rangle|) \quad (7)$$

to measure the distance between two GS's in \mathcal{H} .

To capture the distribution of $\{|\psi^\alpha\rangle\}$ by that of $\{\mathbf{y}^\alpha\}$, we directly optimize $\{\mathbf{y}^\alpha\}$ so that the difference between two probability distributions $\{P(D_{\alpha,\alpha'}^{\mathcal{H}})\}$ and $\{P(D_{\alpha,\alpha'}^{\mathcal{R}})\}$ (averaging over all possible pairs) is minimized. The DR map is left implicit. Consequently, the converged vectors $\{\mathbf{y}^\alpha\}$ represent the quantum states $\{|\psi^\alpha\rangle\}$ in the 2D feature space of reduced dimensionality.

III. IDENTIFYING QUANTUM PHASES IN SPIN MODELS BY VISUALIZATION

A. Landau-type phase transition in 1D transverse field Ising spin chain

We firstly examine our proposal on the 1D transverse field Ising model (TFIM) [32], where the Hamiltonian reads $\hat{H}(h_x) = \sum_i \hat{S}_i^z \hat{S}_{i+1}^z - h_x \sum_i \hat{S}_i^x$, where \hat{S}_i^z and \hat{S}_i^x stand for the z - and x -component spin operators, respectively, and h_x

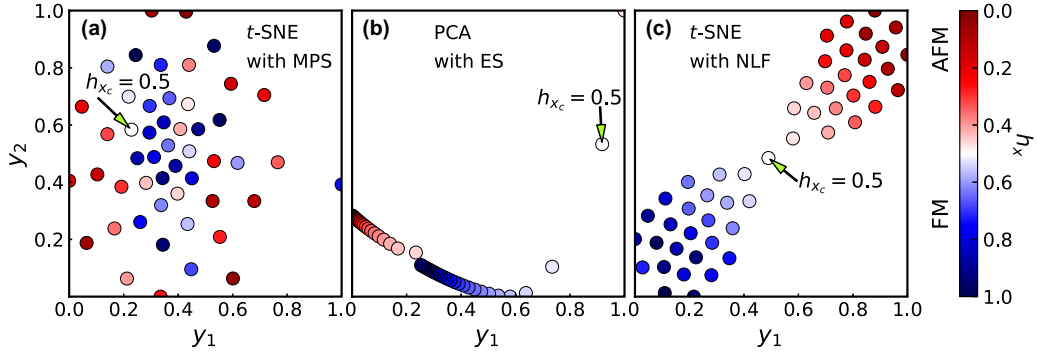


FIG. 2. The visualizations of distinct quantum phases of the 1D transverse field Ising model in two-dimensional feature space \mathcal{R}^2 for three different measuring distances between quantum states. In panel (a), the map is implemented by t -SNE where the distances of states are measured by the Euclidean distances $D_{\alpha,\alpha'}^{\mathcal{M}} = \|\mathbf{v}^\alpha - \mathbf{v}^{\alpha'}\|$ of the MPS parameters. In panel (b), we use PCA for mapping and the entanglement spectra [16] for measuring the distances of states. Panel (c) shows the results of our proposal, where the map is implemented by t -SNE with negative logarithmic fidelity (NLF) $D_{\alpha,\alpha'}^{\mathcal{H}} = -\log(|\langle \psi^\alpha | \psi^{\alpha'} \rangle|)$ as the distance between the ground state. The antiferromagnetic (AFM) and polarized ferromagnetic (FM) phases are clearly specified. Each state is represented by a point on a plane of two components (y_1, y_2) in space \mathcal{R}^2 , and the color bar indicates the magnitudes of h_x . We calculate 50 GS's at different h_x by DMRG, where the values of h_x are taken uniformly from 0 to 1. For DMRG, we take the size of the system $L = 80$ and the dimension cutoff $\chi = 30$. For t -SNE, we take the number of iteration steps $n_{\text{iter}} = 5000$ and the perplexity $\mathcal{P} = 24$.

is the transverse field. It has been rigorously shown that a Landau-type quantum phase transition occurs at the critical field $h_x^c = 0.5$, which separates the antiferromagnetic (AFM) from polarized ferromagnetic (FM) phases. We employ the density matrix renormalization group (DMRG) [33] to calculate the GS's for different transverse fields in the form of matrix product states (MPS) [34–38]. The visualizations of quantum phases of the 1D TFIM using three distinct schemes are presented in Fig. 2.

In Fig. 2(a), we choose the distance between two GS's as the Euclidean distance $D_{\alpha,\alpha'}^{\mathcal{M}} = \|\mathbf{v}^\alpha - \mathbf{v}^{\alpha'}\|$ for comparison, where the vector \mathbf{v}^α is simply formed by all variational parameters in corresponding MPS (i.e., all tensor elements). The t -SNE is used to reduce the dimensionality from \tilde{N} to 2 with \tilde{N} the total number of tensor elements in the MPS. We adopt the canonical form [39] to fix the gauge degrees of freedom of the MPS. It is known that MPS can give an efficient parametrization of the exponentially-large number of GS's of the Hamiltonian under study, where \tilde{N} scales only linearly with the system size [40]. However, our results show that the states after DR are mixed up in \mathcal{R}^2 . It suggests that such a parametrization may not reflect well the quantum state distribution in \mathcal{H} .

In Fig. 2(b), we pick the bipartite entanglement spectra (ES) \mathbf{s}^α of the GS's as the input data, which is χ -dimensional with χ the dimension cutoff in DMRG. Then these ES are mapped onto \mathcal{R}^2 by means of PCA [9–13,41]. Different from the t -SNE, the PCA uses a linear transformation for DR and obtains the two components in \mathcal{R}^2 that optimally retain the covariances of the data in original space. PCA succeeds in identifying the phase transitions of the classical spin models based on the sampled spin configurations by Monte Carlo methods [10–13]. However, for quantum many-body system, it is hardly to directly input the quantum states to PCA due to its exponentially large Hilbert space. One way for classifying the quantum states by PCA is to input the ES of the quantum states [16], where ES is viewed as the effective feature of quantum states. The states from the two phases form a 1D

stream in \mathcal{R}^2 with a break corresponding to the region near the transition point. Our results by PCA are in accordance with those on the Kitaev chain [16]. As indicated in Fig. 2(b), it is not easy to identify the critical point from the distribution of ES with reduced dimensionality by PCA, possibly due to the absence of the nonlinearity in the map between \mathcal{H} and \mathcal{R}^2 .

Figure 2(c) demonstrates the results using our proposal, in which the t -SNE is applied to reduce nonlinearly the dimensionality based on the NLF's [Eq. (7)]. It is obvious that the states inside the AFM and FM phases cluster, and the distribution in \mathcal{R}^2 exhibits an “hourglass” pattern formed by two oval regions. The critical point between the AFM and FM phases can be easily identified by naked eyes (or by unsupervised learning methods where the two ovals touch each other). In previous works, t -SNE has been used to classify phases of both the classical spin models [11] and quantum many-body models [14]. Monte Carlo samplings in a given basis are required to obtain the data for implementing DR. The distances among the quantum states are estimated by Euclidean distances among the sampled (classical) configurations, instead of the states themselves. In this work, we choose NLF to measure the distances. NLF can be efficiently calculated using TN representation, where Monte Carlo samplings are not required. The relevant stochastic errors in the sampling processes can therefore be avoided. The result in Fig. 2(c) indicates that the NLF is a more proper choice for measuring the distance between two GS's in reducing the dimensionality. The convergence and robustness against small noises of the t -SNE with NLF for the visualization of quantum states and phase transitions as well as for the classical data are presented in Sec. V.

B. Identifying multiple phases in XXZ spin chain

Determining the critical points of more than two phases is challenging with the existing machine-learning-based methods such as confusion [16]. We consider the 1D spin- $\frac{1}{2}$ anisotropic XXZ model $\hat{H}(\Delta) = \sum_i (\hat{S}_i^x \hat{S}_{i+1}^x +$

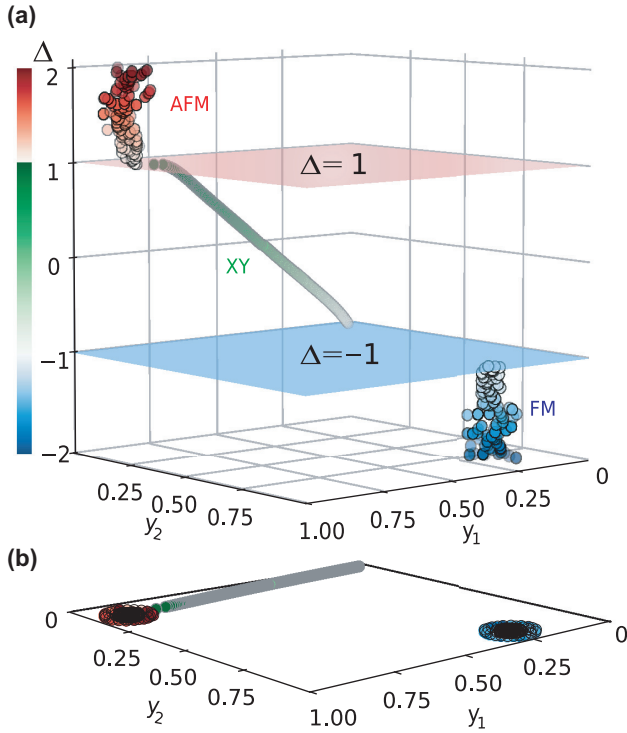


FIG. 3. (a) The three-dimensional (3D) visualization of distinct phases in the 1D anisotropic XXZ antiferromagnetic (AFM) Heisenberg model with anisotropy Δ . In addition to the two dimensions of features y_1 and y_2 of \mathcal{R}^2 , Δ is also plotted as the third dimension for a better visualization. Two expected transition points at $\Delta = -1$ and 1 are indicated by two semitransparent planes to assist visualization. (b) The visualization of panel (a) in feature space \mathcal{R}^2 . Three phases (AFM, XY and FM) are clearly visualized with different patterns in the 3D or 2D space. There are 400 ground states calculated by discretizing Δ with an interval 0.01. We take the system size $L = 120$, the dimension cutoff of DMRG $\chi = 160$, iteration steps in t -SNE $n_{\text{iter}} = 5000$ with the perplexity $\mathcal{P} = 24$.

$\hat{S}_i^y \hat{S}_{i+1}^y + \Delta \sum_i \hat{S}_i^z \hat{S}_{i+1}^z$ [42] with Δ representing the magnetic anisotropy. This system possesses three phases, say FM ($\Delta < -1$), XY ($-1 < \Delta < 1$), and AFM phases ($\Delta > 1$) [42]. Figure 3(a) shows the visualization of the quantum phases of this model in the space spanned by feature y_1 , feature y_2 , and the anisotropy parameter Δ . The expected transition points $\Delta = -1$ and $\Delta = 1$ are indicated by two semitransparent planes. While the states in the FM or AFM phase cluster within the two oval regions of \mathcal{R}^2 [see Fig. 3(b)], the states in the XY phase form a 1D stream. The phase transition points can be accurately identified as the end points of this stream, which touch on the $\Delta = 1$ and -1 planes, respectively.

Recall that for the TFIM, the gapped FM and AFM phases are separated by a critical point at $h_x = 0.5$. The states in the two phases cluster into two ovals in the feature space, where the touching point corresponds to the critical point. Different from the XXZ model, the FM and AFM phases are connected not by a point but a finite region $-1 < \Delta < 1$, in which the system is in a gapless XY phase. We may observe that a 1D stream corresponding to such a gapless region appears, and consequently the two ovals are separated.

C. Topological-to-magnetic phase transitions in spin-1 chains

To further demonstrate the visualized patterns and the identification of phase transitions by our proposal, we turn to the spin-1 antiferromagnetic Heisenberg uniform chain in a magnetic field (h_z), where the Hamiltonian reads $\hat{H}(h_z) = \sum_i \sum_{\kappa=x,y,z} \hat{S}_i^\kappa \hat{S}_{i+1}^\kappa - h_z \sum_i \hat{S}_i^z$. For $h_z < h_{c1}$ with the transition point $h_{c1} \simeq 0.414$, the system is in a topological phase known as Haldane phase [43–46] with nontrivial boundary excitations and long-rang string orders [47–49]. For $h_{c1} < h_z < h_{c2}$ ($h_{c2} = 4$), the system is in a gapless and topologically trivial magnetic phase known as Luttinger liquid (LL) phase [46]. For $h_z > h_{c2}$, the system is in a fully polarized (FP) phase, which is also a gapped phase. As shown in Fig. 4(a), similar patterns as those of the XXZ model appear, where the Haldane, LL, and FP phases are obviously separated. The gapped Haldane and FP phases are visualized as ovals, and the gapless LL phase is visualized as a 1D stream. It should be noted that the visualization of LL phase can be influenced by the number of quantum states sampled therein. Insufficient number of sampled states could result in incorrect visualizations. One simple way to avoid such a potential issue is to check the visualizations with different numbers of states.

Figure 4(b) shows the pattern formed by the GS's of the spin-1 Heisenberg AFM model on zigzag chain with nearest-neighboring (NN) and next-nearest-neighboring (NNN) couplings $\hat{H}(J_1, J_2) = \sum_i \sum_{\kappa=x,y,z} (J_1 \hat{S}_i^\kappa \hat{S}_{i+1}^\kappa + J_2 \hat{S}_i^\kappa \hat{S}_{i+2}^\kappa)$, where J_1 and J_2 denotes the strength of the NN and NNN couplings, respectively. Such a system is frustrated [50] as there is a competition between two kinds of resonating valence bond configurations, of which both possess nontrivial topological properties. A quantum phase transition occurs at $(J_2/J_1)_c \simeq 0.744$ [51], where the system is in the Haldane phase and the NNN Haldane phase on two sides of the critical point. Again, an ‘‘hourglass’’ pattern emerges, where the two phases cluster in two oval areas. The touching point with $J_2/J_1 = 0.745 \pm 0.005$ (the interval of the discretization step $\delta(J_2/J_1) = 0.005$) accurately identifies the transition point.

IV. AUTOMATIC IDENTIFICATION OF QUANTUM PHASES BY K-MEANS

After mapping the ground states to the two-dimensional feature space \mathcal{R}^2 , we show that different quantum phases can be distinguished simply by naked eyes from how the quantum states are distributed in \mathcal{R}^2 . Below, we show that one may use k -means algorithm [28] to classify the states based on the distributions in \mathcal{R}^2 .

K -means method is an unsupervised learning algorithm and can be used to implement classification tasks. For a set of samples $\{\mathbf{y}^\alpha\}$, k -means partitions them into K clusters $\{\mathbb{S}^k\}$ with $k = 1, \dots, K$. The center of each cluster (denoted as $\{\mathbf{m}^k\}$; also called the centroids) can be defined by the samples therein as

$$\mathbf{m}^k = \frac{1}{N^k} \sum_{\mathbf{y}^\alpha \in \mathbb{S}^k} \mathbf{y}^\alpha, \quad (8)$$

where N^k is the number of samples in \mathbb{S}^k .

To classify $\{\mathbf{y}^\alpha\}$, one performs the following two steps iteratively. The first step is to assign the samples to the K

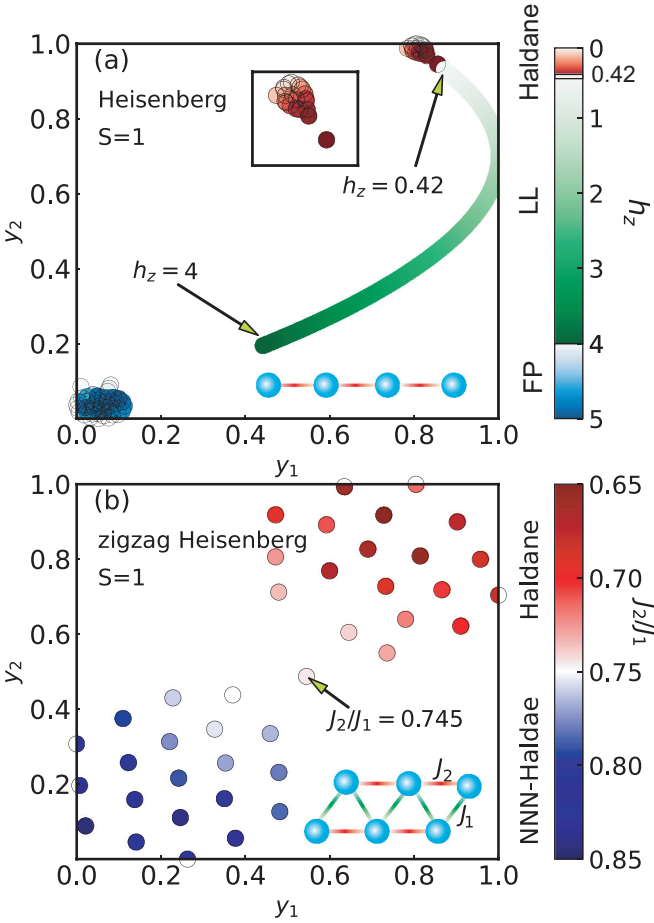


FIG. 4. The visualization of quantum phases in the spin-1 Heisenberg chain (a) in different magnetic field h_z , and (b) the visualization of those of the spin-1 Heisenberg antiferromagnetic zigzag chain with different strength of the next-nearest neighboring (NNN) couplings J_2/J_1 (the nearest neighboring coupling is fixed at 1). In panel (a), the Haldane phase Luttinger liquid (LL) phase and fully polarized (FP) phase are clearly specified, where it gives the critical field $h_{z1} = 0.42 \pm 0.02$, and $h_{z2} = 4 \pm 0.02$. In panel (b), the two distinct Haldane phases are obviously separated, which shows the critical NNN coupling $(J_2/J_1) = 0.745 \pm 0.005$. The distance of quantum states is measured by $D_{\alpha, \alpha'}^H = -\log(|\langle \psi^\alpha | \psi^{\alpha'} \rangle|)$. We take 250 values of h_z and 40 values of J_2/J_1 with the interval $\delta h = 0.02$ and $\delta J_2/J_1 = 0.005$ for the two models, respectively. We take the system size $L = 128$ and 100, the dimension cutoff of DMRG $\chi = 128$ and 60 for panels (a) and (b), respectively. Iterative steps in t -SNE $n_{\text{iter}} = 5000$ with the perplexity $\mathcal{P} = 20$ for both.

clusters according to the given $\{\mathbf{m}^k\}$, where any sample in a given cluster should possess the smallest Euclidean distance to the center of this cluster than to other centers. It means that the samples are divided into K sets $\{S^k\}$ by satisfying

$$S^k = \{\mathbf{y}^\alpha : \|\mathbf{y}^\alpha - \mathbf{m}^k\| \leq \|\mathbf{y}^\alpha - \mathbf{m}^j\| \forall j\}, \quad (9)$$

where $\|\mathbf{y}^\alpha - \mathbf{m}^k\|$ represents the Euclid distance between the sample \mathbf{y}^α and the center \mathbf{m}^k , and j goes over all centers. The second step is to update $\{\mathbf{m}^k\}$ based on the present $\{S^k\}$ according to Eq. (8). These two steps are executed iteratively until $\{\mathbf{m}^k\}$ converges.

We apply k -means to categorize the ground states of spin-1 antiferromagnetic Heisenberg chain into two phases ($K = 2$) after mapping those states onto \mathcal{R}^2 space by t -SNE. In Fig. 5, the numbers represent the ground states with reduced dimensionality $\{\mathbf{y}^\alpha\}$ in different magnetic fields α , and the two stars represent the centers $\{\mathbf{m}^k\}$. The states divided into two clusters are marked by different colors. To begin with, one first randomly initializes the positions of the centers, with which the states are divided into two clusters according to Eq. (9). After four steps of iterations, $\{\mathbf{m}^k\}$ converges, and the states in different phases are successfully divided to the two clusters. Figure 5(f) shows how the centers converge by making use of

$$D(n_{\text{it}}) = \sum_k^K \|\mathbf{m}^k(n_{\text{it}}) - \mathbf{m}^k(n_{\text{it}} - 1)\|, \quad (10)$$

with $\{\mathbf{m}^k(t)\}$ the centers after t iterations. We find that $D(t)$ decreases almost to 0 for $n_{\text{it}} = 4$.

Though K is previously known in the above example, it can also be determined automatically when one does not know how many clusters that the samples should be divided into. We refer to the silhouette coefficient (SC) [52] and Calinski-Harabasz index (CHI) [53,54] for this purpose. The SC is defined as

$$\text{SC} = \frac{1}{J} \sum_{\alpha=1}^J \frac{\overline{D}_{\text{out}}^\alpha - \overline{D}_{\text{in}}^\alpha}{\max(\overline{D}_{\text{out}}^\alpha, \overline{D}_{\text{in}}^\alpha)}, \quad (11a)$$

$$\overline{D}_{\text{in}}^\alpha = \frac{1}{N^{k(\alpha)} - 1} \sum_{\mathbf{y}^{\alpha'} \in S^{k(\alpha)}} \|\mathbf{y}^{\alpha'} - \mathbf{y}^\alpha\|, \quad (11b)$$

$$\overline{D}_{\text{out}}^\alpha = \frac{1}{N - N^{k(\alpha)}} \sum_{\mathbf{y}^{\alpha'} \notin S^{k(\alpha)}} \|\mathbf{y}^{\alpha'} - \mathbf{y}^\alpha\|, \quad (11c)$$

where $k(\alpha)$ represents the cluster that the α th data point belongs to, $\overline{D}_{\text{in}}^j$ ($\overline{D}_{\text{out}}^j$) is the average distance of sample j to others in (not in) the same cluster. The value of SC ranges from -1 to 1 . The optimal K is chosen so that $\text{SC} \rightarrow 1$ [52].

The CHI is defined as [53]

$$\text{CHI} = \frac{\text{Trace}(B)/(K-1)}{\text{Trace}(W)/(J-K)}, \quad (12a)$$

$$\text{Trace}(B) = \sum_{k=1}^K N^k \|\mathbf{m}^k - \mathbf{m}^0\|^2, \quad (12b)$$

$$\text{Trace}(W) = \sum_{k=1}^K \sum_{\mathbf{y}^\alpha \in S^{k(\alpha)}} \|\mathbf{y}^\alpha - \mathbf{m}^k\|^2. \quad (12c)$$

B is the between-cluster scatter matrix and W is the within-cluster scatter matrix; \mathbf{m}^0 is the centroid of the whole dataset. The optimal K is chosen so that CHI reaches its maximum [53].

For the ground states of the spin $S = 1$ antiferromagnetic Heisenberg uniform chain and zigzag chain, Fig. 6 shows the SC and CHI calculated from the distribution of the ground states in \mathcal{R}^2 . One can see that the optimal number of clusters should be $K = 2$, consistent with the fact that there are two phases for each system. In this way, one does not need priori

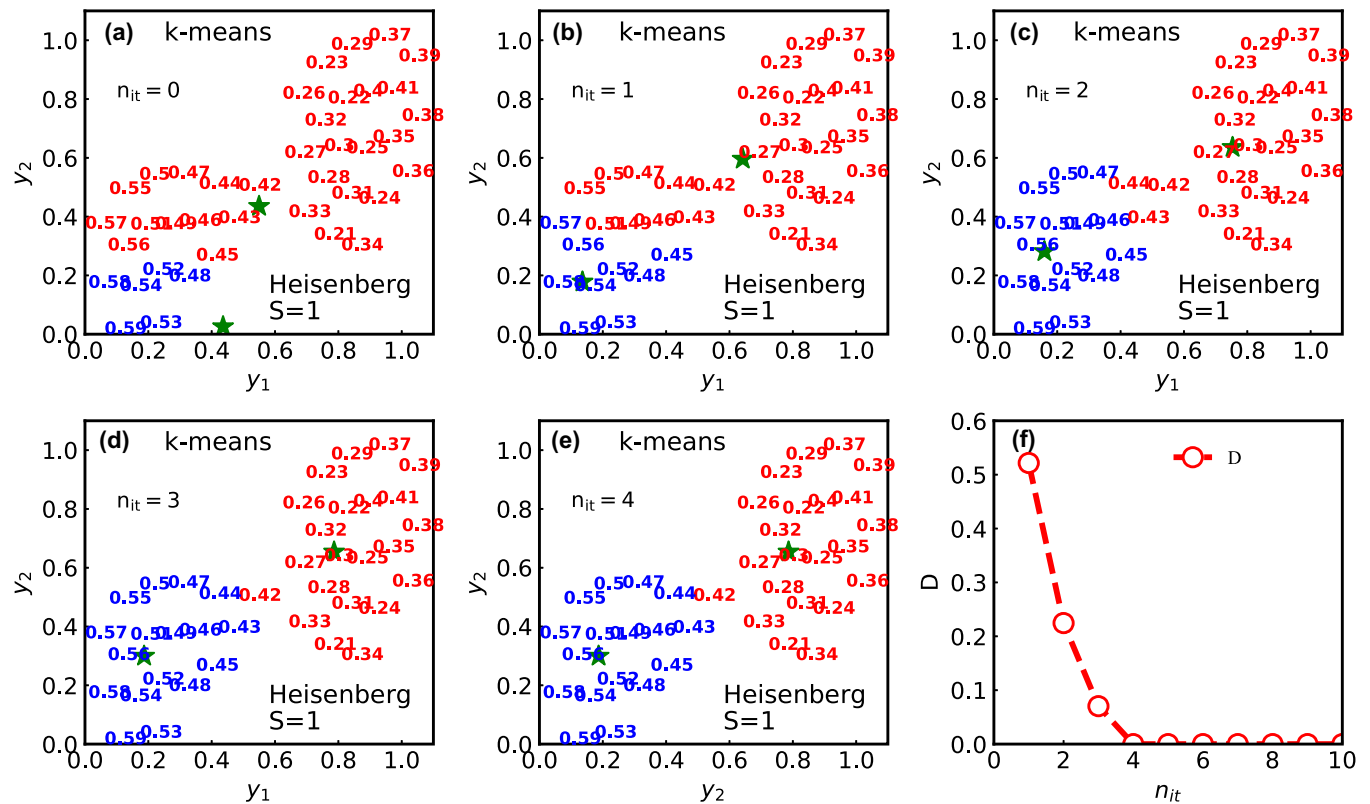


FIG. 5. Panels (a)-(e) demonstrate the evolution of samples classified into different clusters (marked by red or blue) and the centers of clusters (indicated by the two stars) after different iteration time in k -means. The numbers in panels (a)-(e) denote the magnitudes of the applied magnetic fields. **f** shows the difference of the centers before and after the n_{it} th iteration [see Eq. (10)], showing that the iteration converges only after $n_{it} = 4$ steps.

knowledge about either the properties of the original states or the number of phases.

V. ROBUSTNESS OF T -SNE FOR QUANTUM PHASE IDENTIFICATION

Fig. 7 show in t -SNE, how the distribution in \mathcal{R}^2 of the ground states of the transverse field Ising model converges. Remind that for N given states $|\psi^\alpha\rangle$ in the Hilbert space \mathcal{H} , the t -SNE directly optimizes \mathbf{y}^α in \mathcal{R}^2 that are the N corresponding low-dimensional vectors after reducing the dimensionality. Initially, \mathbf{y}^α are randomly determined. Figures 7(a)–7(e) show the \mathbf{y}^α after n_{it} iterations with $n_{it} =$

250, 300, 350, 400, 500, respectively. One can see that after $n_{it} \simeq 400$ iterations, the distribution converges, where the two quantum phases are clearly visualized. The KL divergence, which indicates the difference between the distributions of the samples in \mathcal{H} and \mathcal{R}^2 , decays with n_{it} as shown in Fig. 7(f). A GIF was provided [55] to animatedly show how the states cluster in \mathcal{R}^2 as the iteration time increases.

From the previous works in machine learning, it is known that the visualization by t -SNE is robust to the perplexity \mathcal{P} . Figure 8 shows that the ground states of the transverse field Ising model (TFIM) by t -SNE with different perplexities form similar hourglasslike patterns. The difference of these patterns is to what extent the hourglass extends in the two-dimensional plane. This is consistent with the fact that the perplexity controls how nonlocally one state is correlated to others from the joint probability distribution. More specifically, as the dimensionality is reduced, the distribution in \mathcal{R}^2 may not respect the mutual relations among the states in \mathcal{H} . For instance, it is possible that one has $\|\mathbf{y}^1 - \mathbf{y}^2\| < \|\mathbf{y}^1 - \mathbf{y}^3\|$ in \mathcal{H} but $\|\mathbf{y}^1 - \mathbf{y}^2\| > \|\mathbf{y}^1 - \mathbf{y}^3\|$ in \mathcal{R}^2 . A small perplexity means that the distribution in \mathcal{R}^2 should in prior satisfies the mutual relations of distances for those with small distances. Consequently in the visualization with small \mathcal{P} , different clusters tend to separate apart mutually. This leads to a “thinner” hourglass than those with larger perplexities. Note that in practice, the perplexity is usually smaller than the number of samples [26].

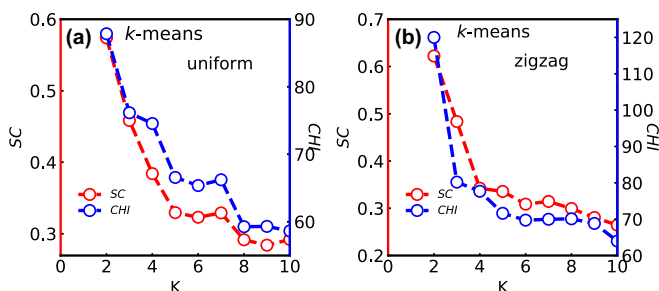


FIG. 6. The SC [Eq. (11a)] and CHI [Eq. (12a)] versus K for the spin $S = 1$ antiferromagnetic Heisenberg uniform chain (a) and zigzag chain (b).

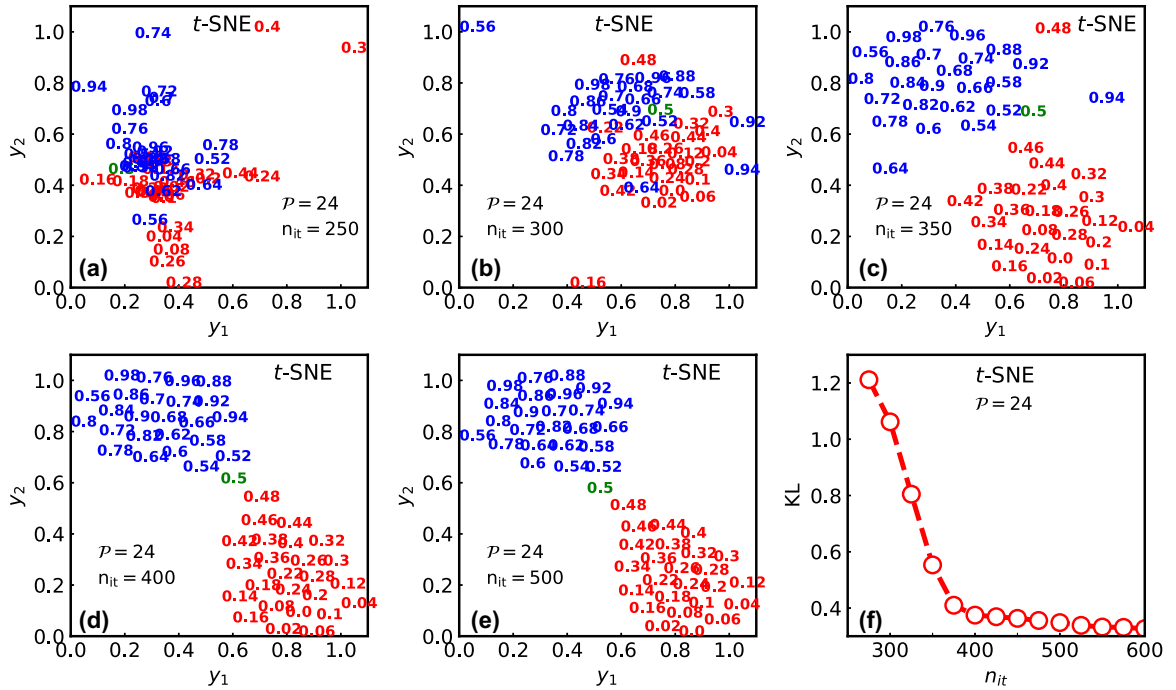


FIG. 7. Distribution of quantum states in 2D feature space varies with iteration time of t -SNE. The distribution in \mathcal{R}^2 of the ground states of TFIM by t -SNE with the iteration time $n_{it} = 250, 300, 350, 400, 500$ in panels (a)-(e), respectively. Panel (f) shows the KL divergence versus n_{it} . Here we take the perplexity $\mathcal{P} = 24$, the system size $L = 80$, and dimension cutoff in DMRG $\chi = 30$. The red and blue numbers represent the applied magnetic fields, and the green number 0.5 denotes the critical field.

We also investigate the visualization of quantum phases under noises. The noisy quantum states are defined by

$$|\Psi_\delta^\alpha\rangle = \sqrt{1-\delta}|\Psi^\alpha\rangle + \sqrt{\delta}|\Psi_{\text{random}}\rangle, \quad (13)$$

where $|\Psi^\alpha\rangle$ is the ground state in the transverse magnetic field α , and δ is a small constant that controls the strength of the noise. $|\Psi_{\text{random}}\rangle$ is a random matrix product state (MPS) whose bond dimensions are identical to those of the ground

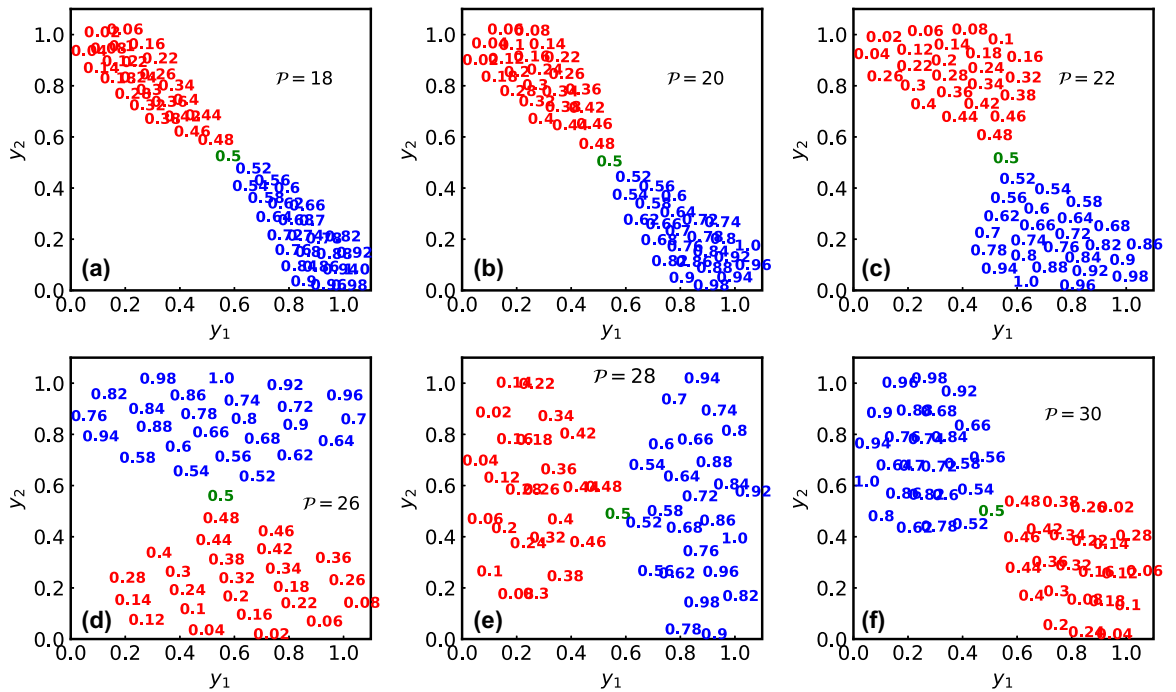


FIG. 8. Distribution of quantum states in 2D feature space varies with perplexities of t -SNE. Visualization of the ground states of TFIM by t -SNE with different perplexities $\mathcal{P} = 18, 20, 22, 26, 28$, and 30 . We take the total iteration times in t -SNE $n_{it} = 5000$, the system size $L = 80$, and dimension cutoff in DMRG $\chi = 30$.

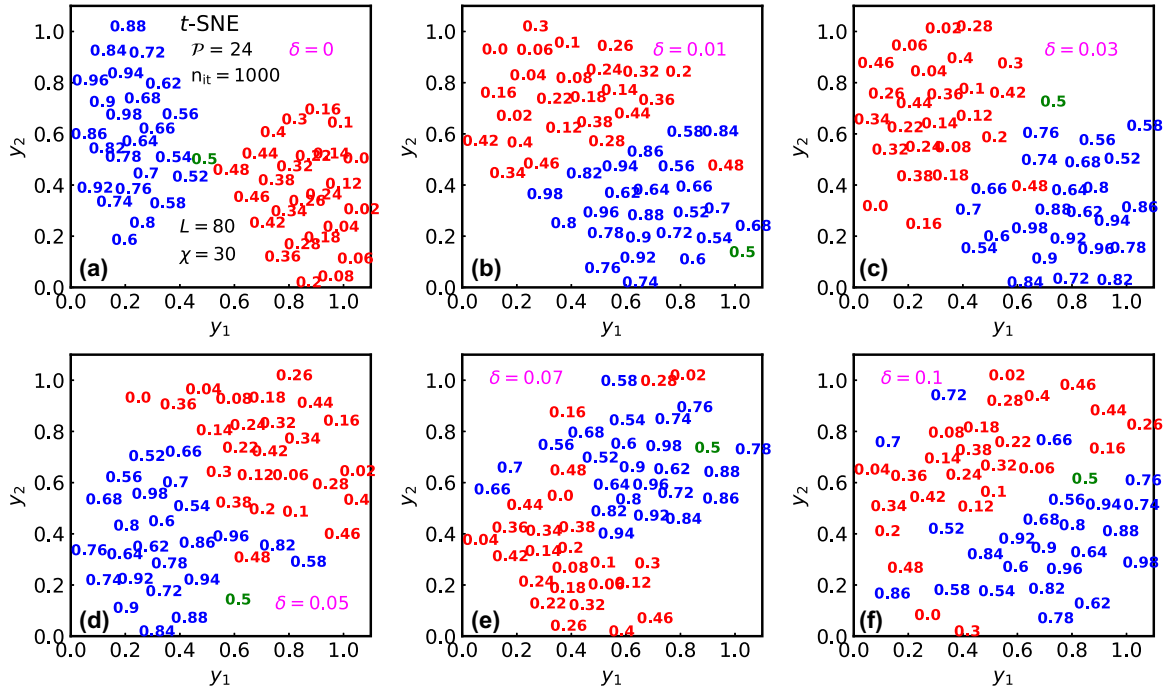


FIG. 9. Distribution of quantum states in 2D feature space varies with noises. The visualization of the ground states of TFIM under small noise by t -SNE with different strengths of noise $\delta = 0, 0.01, 0.03, 0.05, 0.07$, and 0.1 in panels (a)-(f), respectively. We take the perplexity $\mathcal{P} = 24$, the total iteration time $n_{it} = 1000$, the system size $L = 80$, and dimension cutoff in DMRG $\chi = 30$.

states. All elements of the tensors in $|\Psi_{\text{random}}\rangle$ are generated randomly by the Gaussian distribution $N(0, 1)$.

In Fig. 9, we show the visualizations of $\{|\Psi_{\delta}^{h_x}\rangle\}$ with $\delta = 0, 0.01, 0.03, 0.05, 0.07$, and 0.1 . By increasing δ till approximately $\delta = 0.05$, we observe that the states in the two phases still form two clusters which are roughly linearly separable. However, the two clusters gradually merge into each other with continually increasing δ , which becomes more and more difficult to identify the two phases. The separability of the two clusters can effectively reflect whether our scheme could work or not for identifying the quantum phases and to what extent it can tolerate noises. Note that the quantum states are obtained by DMRG, which themselves contain certain numerical noises. These results (including those in Fig. 9) suggest that t -SNE with NLF can resist a small extent noise attack.

VI. VISUALIZATION OF IMAGES WITH QUANTUM FEATURE MAP AND NEGATIVE LOGARITHMIC FIDELITY

Below, we show that our scheme can also be applied to visualize classical data, such as the images in the MNIST [56] and fashion-MNIST [57] datasets. To calculate the negative logarithmic fidelity (NLF) of the classical samples, we firstly map each pixel x_n^{α} to the Hilbert space [58] by

$$|\phi(x_n^{\alpha})\rangle = \cos \frac{\pi x_n^{\alpha}}{4} |0\rangle + \sin \frac{\pi x_n^{\alpha}}{4} |1\rangle, \quad (14)$$

where x_n^{α} with $0 \leq x_n \leq 1$ denotes the value of the n th pixel in the α th image, and $\{|i\rangle\}$ ($i = 0, 1$) denote the orthonormal basis in the two-dimensional Hilbert space. Then an image can

be mapped to a product state as

$$|\psi^{\alpha}\rangle = |\phi(x_1^{\alpha})\rangle \otimes |\phi(x_2^{\alpha})\rangle \otimes \cdots \otimes |\phi(x_n^{\alpha})\rangle. \quad (15)$$

Obviously, $|\psi^{\alpha}\rangle$ is a state defined in the 2^L -dimensional Hilbert space with L the total number of pixels in one image. The NLF between two images is defined as

$$D_{\alpha, \alpha'}^{\mathcal{H}} = -\log(\langle \psi^{\alpha} | \psi^{\alpha'} \rangle). \quad (16)$$

With $D_{\alpha, \alpha'}^{\mathcal{H}}$, the images can be visualized by t -SNE by following the same steps for visualizing the ground states.

The visualizations of the images in MNIST and fashion-MNIST based on NLF are shown in Figs. 10(a) and 10(c), respectively. As a comparison, the visualizations using the Euclidean distance $D_{\alpha, \alpha'}^{\mathcal{E}} = \|\mathbf{x}^{\alpha} - \mathbf{x}^{\alpha'}\|$ in the t -SNE are shown in Fig. 10(b) and 10(d) for MNIST and fashion-MNIST, respectively. Both schemes show similar visualization results, which indicates that our scheme also works well for visualizing classical data.

VII. DISCUSSIONS

Our results show that the states in the gapless (XX and LL) phases are visualized as 1D streams in \mathcal{R}^2 . In contrast, the noncritical phases (the FM/AFM and gapped topological phases) are visualized as oval clusters. To explain the cause of different patterns of the distributions given by the critical and noncritical phases, we propose the following intuitive arguments. Normally the distance of two states (in both \mathcal{H} and \mathcal{R}^2) is positively associated with the difference of their physical quantities (e.g., magnetizations, correlations, entanglement spectrum, etc.). The states within each phase should have small distances among each other.

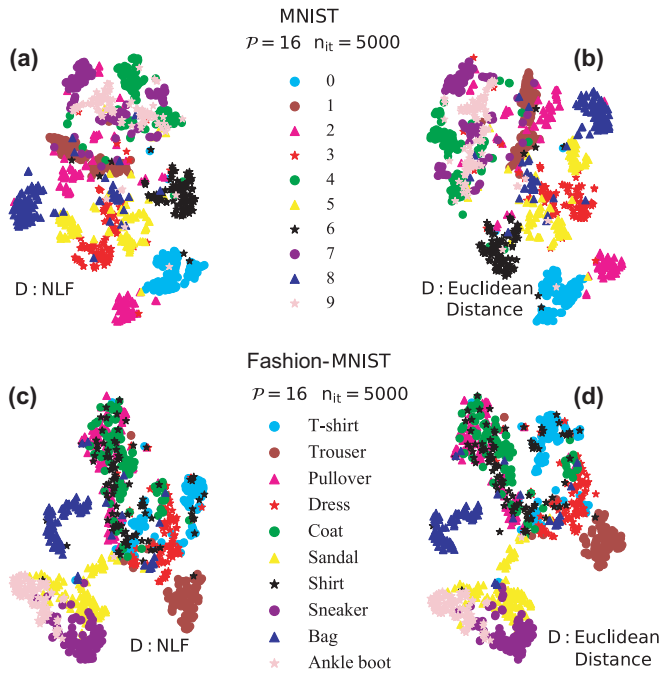


FIG. 10. Visualization of classical datasets by t -SNE with NLF and Euclidean distance. The visualization of the MNIST dataset and the fashion-MNIST dataset by t -SNE with NLF or the Euclidean distance. In panels (a) and (c), the images are mapped onto the Hilbert space, where the distance of two different images are measured by NLF. In panels (b) and (d), the distance of two different images are measured by the Euclidean distance in the original feature space. For both MNIST and Fashion-MNIST datasets, we take 1000 images (100 images from each class) as the input of t -SNE. We take $\mathcal{P} = 16$ and total iteration times $n_{it} = 5000$.

The physics of the states within a gapped phase are almost identical. Consequently, the distances among the states within one same gapped phase are insignificant. Even the energy levels do cross due to finite-size effects or numerical errors, the differences of the physics for these states should be minor. Therefore, the quantum states are expected to cluster in a small region in \mathcal{R}^2 . Take the polarized phase in TFIM as an example. For different h_x 's with $h_x > 0.5$, the distances among the states inside the phase are insignificant compared with the distances between the states in different phases. In the vicinity of the critical point, the gap gradually closes, and the energy levels become dense. Meanwhile, the physical properties change more drastically as the physical parameter alters. It turns out that near a critical point the distances between the quantum states with different parameters become more significant than those within the noncritical phases.

When two noncritical phases are separated by a critical phase instead of a critical point, the distances of the states within the critical phase should be more significant than those within the noncritical phases. This explains the distribution of the 1D pattern of the gapless XY phase in the XXZ model (Fig. 3) and that of the LL phase in the spin-1 Heisenberg chain [Fig. 4(a)].

Our results suggest that the quantum phase transition points can be robustly identified by our scheme without *a priori* knowing the order parameters. Due to the uninterpretability of the nonlinear manifold learning schemes including t -SNE, the relationship between the shapes of different quantum phases and their physical properties is just a speculation at present, and the underlying insight behind this observation is left for our future study. We believe that our work is still a start-up of unveiling the physical properties of quantum phases with the geometries of the patterns given by the ground states with reduced dimensions.

VIII. SUMMARY

In summary, we propose a scheme to visualize quantum phases and to identify phase transition points via machine learning. The key idea is to map the quantum states in Hilbert space \mathcal{H} where the distribution of ground states is difficult to access onto the 2D feature space \mathcal{R}^2 by the nonlinear DR method t -SNE, where the negative logarithmic fidelity is adopted to measure the distances between different quantum states. It is found that the distribution in \mathcal{R}^2 exhibits different patterns for distinct phases, from which the phase transition points can be readily identified. The success of this proposal is demonstrated on a few of 1D quantum many-body models, including those with conventional phases within Landau paradigm, the topological phases with nonlocal orders, and the critical phase described by CFT. This present strategy for visualization through learning works well not only for quantum data but also for classical data.

While our scheme of visualizing quantum phases via learning are flexible and general, more rigorous and robust relations between the distributions in \mathcal{R}^2 and the physical properties of the quantum phases (e.g., criticality and topology) space are to be established. As a nonlinear DR method, the t -SNE works as a “black box” which guarantees the minimization of the KL-divergence in a variational sense, and it is unknown how to interpret it, for instance, what the two features (y_1 and y_2 in \mathcal{R}^2) stand for. It is really interesting to seek for the DR methods with higher interpretability, which would assist us to unveil more novel properties of quantum many-body systems by this visualization scheme.

ACKNOWLEDGMENTS

This work is supported in part by the NSFC (Grant No. 11834014), the National Key R&D Program of China (Grant No. 2018YFA0305800), the Strategic Priority Research Program of the Chinese Academy of Sciences (Grant No. XDB28000000), and Beijing Municipal Science and Technology Commission (Grant No. Z190011). S.J.R. is supported by NSFC (Grant No. 12004266), Beijing Natural Science Foundation (Grants No. 1192005 and No. Z180013), Foundation of Beijing Education Committees (Grant No. KM202010028013), and the Academy for Multidisciplinary Studies, Capital Normal University.

- [1] L. D. Landau, On the theory of phase transitions, *Ukr. J. Phys.* **11**, 19 (1937).
- [2] V. L. Ginzburg and L. D. Landau, On the theory of superconductivity, in *On Superconductivity and Superfluidity* (Springer, Berlin, 2009), pp. 113–137.
- [3] X.-G. Wen, Vacuum degeneracy of chiral spin states in compactified space, *Phys. Rev. B* **40**, 7387 (1989).
- [4] X. Chen, Z.-C. Gu, and X.-G. Wen, Local unitary transformation, long-range quantum entanglement, wave function renormalization, and topological order, *Phys. Rev. B* **82**, 155138 (2010).
- [5] G. Carleo and M. Troyer, Solving the quantum many-body problem with artificial neural networks, *Science* **355**, 602 (2017).
- [6] J. Carrasquilla and R. G. Melko, Machine learning phases of matter, *Nat. Phys.* **13**, 431 (2017).
- [7] P. Broecker, J. Carrasquilla, R. G. Melko, and S. Trebst, Machine learning quantum phases of matter beyond the fermion sign problem, *Sci. Rep.* **7**, 8823 (2017).
- [8] K. Ch'ng, J. Carrasquilla, R. G. Melko, and E. Khatami, Machine Learning Phases of Strongly Correlated Fermions, *Phys. Rev. X* **7**, 031038 (2017).
- [9] K. Pearson, Liii. on lines and planes of closest fit to systems of points in space, *Philos. Mag.* **2**, 559 (1901).
- [10] L. Wang, Discovering phase transitions with unsupervised learning, *Phys. Rev. B* **94**, 195105 (2016).
- [11] S. J. Wetzel, Unsupervised learning of phase transitions: From principal component analysis to variational autoencoders, *Phys. Rev. E* **96**, 022140 (2017).
- [12] W. Hu, R. R. P. Singh, and R. T. Scalettar, Discovering phases, phase transitions, and crossovers through unsupervised machine learning: A critical examination, *Phys. Rev. E* **95**, 062122 (2017).
- [13] C. Wang and H. Zhai, Machine learning of frustrated classical spin models. I. Principal component analysis, *Phys. Rev. B* **96**, 144432 (2017).
- [14] K. Ch'ng, N. Vazquez, and E. Khatami, Unsupervised machine learning account of magnetic transitions in the Hubbard model, *Phys. Rev. E* **97**, 013306 (2018).
- [15] E. Khatami, E. Guardado-Sanchez, B. M. Spar, J. F. Carrasquilla, W. S. Bakr, and R. T. Scalettar, Visualizing strange metallic correlations in the two-dimensional Fermi-Hubbard model with artificial intelligence, *Phys. Rev. A* **102**, 033326 (2020).
- [16] E. P. L. Van Nieuwenburg, Y.-H. Liu, and S. D. Huber, Learning phase transitions by confusion, *Nat. Phys.* **13**, 435 (2017).
- [17] J. F. Rodriguez-Nieva and M. S. Scheurer, Identifying topological order through unsupervised machine learning, *Nat. Phys.* **15**, 790 (2019).
- [18] W. Zhang, J. Liu, and T.-C. Wei, Machine learning of phase transitions in the percolation and xy models, *Phys. Rev. E* **99**, 032142 (2019).
- [19] M. S. Scheurer and R.-J. Slager, Unsupervised Machine Learning and Band Topology, *Phys. Rev. Lett.* **124**, 226401 (2020).
- [20] Y. Long, J. Ren, and H. Chen, Unsupervised Manifold Clustering of Topological Phononics, *Phys. Rev. Lett.* **124**, 185501 (2020).
- [21] Y. Che, C. Gneiting, T. Liu, and F. Nori, Topological quantum phase transitions retrieved through unsupervised machine learning, *Phys. Rev. B* **102**, 134213 (2020).
- [22] J. A. Lee and M. Verleysen, *Nonlinear Dimensionality Reduction* (Springer-Verlag, New York, 2007).
- [23] B. Mokbel, W. Lueks, A. Gisbrecht, and B. Hammer, Visualizing the quality of dimensionality reduction, *Neurocomputing* **112**, 109 (2013).
- [24] J. B. Tenenbaum, V. De Silva, and J. C. Langford, A global geometric framework for nonlinear dimensionality reduction, *Science* **290**, 2319 (2000).
- [25] G. E. Hinton and S. T. Roweis, Stochastic neighbor embedding, in *Advances in Neural Information Processing Systems 15*, edited by S. Becker, S. Thrun, and K. Obermayer (MIT Press, Cambridge, MA, 2003), pp. 857–864.
- [26] Laurens van der Maaten and G. Hinton, Visualizing data using t-SNE, *J. Mach. Learn. Res.* **9**, 2579 (2008).
- [27] P. Huembeli, A. Dauphin, and P. Wittek, Identifying quantum phase transitions with adversarial neural networks, *Phys. Rev. B* **97**, 134109 (2018).
- [28] H.-P. Kriegel, P. Kröger, J. Sander, and A. Zimek, Density-based clustering, *Data Min. Knowl. Discov.* **1**, 231 (2011).
- [29] S. Kullback and R. A. Leibler, On information and sufficiency, *Ann. Math. Statist.* **22**, 79 (1951).
- [30] H.-Q. Zhou, R. Orús, and G. Vidal, Ground-State Fidelity from Tensor Network Representations, *Phys. Rev. Lett.* **100**, 080601 (2008).
- [31] M. M. Rams and B. Damski, Quantum Fidelity in the Thermodynamic Limit, *Phys. Rev. Lett.* **106**, 055701 (2011).
- [32] E. Lieb, T. Schultz, and D. Mattis, Two soluble models of an antiferromagnetic chain, *Ann. Phys.* **16**, 407 (1961).
- [33] S. R. White, Density Matrix Formulation for Quantum Renormalization Groups, *Phys. Rev. Lett.* **69**, 2863 (1992).
- [34] M. Fannes, B. Nachtergaele, and R. F. Werner, Exact antiferromagnetic ground states of quantum spin chains, *Europhys. Lett.* **10**, 633 (1989).
- [35] M. Fannes, B. Nachtergaele, and R. F. Werner, Finitely correlated states on quantum spin chains, *Commun. Math. Phys.* **144**, 443 (1992).
- [36] D. Perez-Garcia, F. Verstraete, M. M. Wolf, and J. I. Cirac, Matrix product state representations, *Quantum Info. Comput.* **7**, 401 (2007).
- [37] F. Verstraete, V. Murg, and J. I. Cirac, Matrix product states, projected entangled pair states, and variational renormalization group methods for quantum spin systems, *Adv. Phys.* **57**, 143 (2008).
- [38] S.-J. Ran, E. Tirrito, C. Peng, Xi Chen, L. Tagliacozzo, G. Su, and M. Lewenstein, Tensor network contraction and multilinear algebra, *Lect. Notes Phys.* **964**, 99 (2020).
- [39] R. Orús and G. Vidal, Infinite time-evolving block decimation algorithm beyond unitary evolution, *Phys. Rev. B* **78**, 155117 (2008).
- [40] F. Verstraete and J. I. Cirac, Matrix product states represent ground states faithfully, *Phys. Rev. B* **73**, 094423 (2006).
- [41] N. C. Costa, W. Hu, Z. J. Bai, R. T. Scalettar, and R. R. P. Singh, Principal component analysis for fermionic critical points, *Phys. Rev. B* **96**, 195138 (2017).
- [42] T. Giamarchi, *Quantum Physics in One Dimension* (Clarendon Press, Oxford, UK, 2003), Vol. 121.
- [43] F. D. M. Haldane, Continuum dynamics of the 1D Heisenberg antiferromagnet: Identification with the $O(3)$ nonlinear sigma model, *Phys. Lett. A* **93**, 464 (1983).

- [44] F. D. M. Haldane, Nonlinear Field Theory of Large-Spin Heisenberg Antiferromagnets: Semiclassically Quantized Solitons of the One-Dimensional Easy-Axis Néel State, *Phys. Rev. Lett.* **50**, 1153 (1983).
- [45] S. R. White and D. A. Huse, Numerical renormalization-group study of low-lying eigenstates of the antiferromagnetic $s = 1$ heisenberg chain, *Phys. Rev. B* **48**, 3844 (1993).
- [46] T. Sakai and M. Takahashi, Anisotropic $s = 1$ antiferromagnetic Heisenberg chain in a magnetic field, *J. Phys. Soc. Jpn.* **62**, 750 (1993).
- [47] M. den Nijs and K. Rommelse, Preroughening transitions in crystal surfaces and valence-bond phases in quantum spin chains, *Phys. Rev. B* **40**, 4709 (1989).
- [48] F. Anfuso and A. Rosch, String order and adiabatic continuity of haldane chains and band insulators, *Phys. Rev. B* **75**, 144420 (2007).
- [49] F. Anfuso and A. Rosch, Fragility of string orders, *Phys. Rev. B* **76**, 085124 (2007).
- [50] L. Balents, Spin liquids in frustrated magnets, *Nature (London)* **464**, 199 (2010).
- [51] A. Kolezhuk, R. Roth, and U. Schollwöck, First Order Transition in the Frustrated Antiferromagnetic Heisenberg $s = 1$ Quantum Spin Chain, *Phys. Rev. Lett* **77**, 5142 (1996).
- [52] P. J. Rousseeuw, Silhouettes: A graphical aid to the interpretation and validation of cluster analysis, *J. Comput. Appl. Math.* **20**, 53 (1987).
- [53] U. Maulik and Sanghamitra Bandyopadhyay, Performance evaluation of some clustering algorithms and validity indices, *IEEE Trans. Pattern Anal. Mach. Intell.* **24**, 1650 (2002).
- [54] J. Wang, W. Zhang, T. Hua, and T.-C. Wei, Unsupervised learning of topological phase transitions using Calinski-Harabaz index, *Phys. Rev. Research* **3**, 013074 (2021).
- [55] Visualizing process of quantum states, <https://github.com/yangyuan16/QSvisualization>.
- [56] L. Deng, The mnist database of handwritten digit images for machine learning research [best of the web], *IEEE Signal Process. Mag.* **29**, 141 (2012).
- [57] H. Xiao, K. Rasul, and R. Vollgraf, Fashion-MNIST: A novel image dataset for benchmarking machine learning algorithms, [arXiv:1708.07747](https://arxiv.org/abs/1708.07747) (2017).
- [58] E. Stoudenmire and D. J. Schwab, Supervised learning with tensor networks, in *Advances in Neural Information Processing Systems* (Curran Associates, Red Hook, NY, 2016), pp. 4799–4807.